Journal of Materials Chemistry B

ROYAL SOCIETY OF CHEMISTRY

COMMUNICATION

View Article Online
View Journal | View Issue

Cite this: J. Mater. Chem. B, 2023, 11, 4389

Received 9th March 2023,
Accepted 11th April 2023

DOI: 10.1039/d3tb00510k

rsc.li/materials-b

Water-soluble polymer brush-substituted squaraine NIR-II dye for efficient photothermal therapy†

Xiaoli Li,[a] Song Guo,[a] Weixing Deng,*[a] Si Wu,[ac] Pengfei Sun*[b] and Yuanli Liu*[a]

Near-infrared II (NIR-II, 1000–1700 nm) fluorescence imaging has the advantages of low light scattering and weak biological autofluorescence compared with conventional NIR (600–900 nm) fluorescence imaging and can obtain a high signal-to-noise ratio in deeper biological tissues, as well as micron-level high resolution. A great deal of effort has been directed toward the construction of conjugated polymers for effective NIR-triggered fluorescence imaging (FI) and photothermal therapy (PTT) combined therapy. However, NIR-II fluorescent materials are mainly nanoparticles prepared by coprecipitation methods, and water-soluble NIR-II materials need to be further developed. In this paper, we synthesized novel water-soluble squaric acid nanoparticles (SQ-POEGMA) with low toxicity and excellent photostability by attaching a water-soluble oligomer (POEGMA) to the small molecule squaric acid through a click chemistry reaction. The photothermal conversion efficiency of SQ-POEGMA is 33% *in vitro*, which can effectively inhibit the growth of cancer cells with 94% tumor inhibition rate *in vivo* under 808 nm laser irradiation, while no appreciable side effects were observed.

Cancer has become a serious threat to humans worldwide due to its high morbidity, which is closely linked to the highly invasive and metastatic ability and mortality rates,[1] and most patients are already in an advanced stage of treatment. Therefore, early diagnosis and treatment of tumors are important to improve the cure rate, reduce the cost of treatment and reduce the financial burden on patients.[2]

Currently, the traditional imaging diagnosis for tumors mainly includes electronic computed tomography (CT), magnetic resonance imaging (MRI) and ultrasound imaging.[3–6] However, the above imaging tools still have some shortcomings. For example, CT will bring a high risk of radiation and cannot be imaged in real time, and both MRI and CT are expensive. Low-cost ultrasound imaging can be performed in real time but with low resolution. Optical imaging is an important imaging technique that shows great potential in the biomedical field because of its advantages of low damage to living organisms and high spatiotemporal resolution.[7–10] Light penetration and sensitivity reduced because of the absorption and scattering of endogenous substances such as melanin, haemoglobin, deoxyhemoglobin, and bilirubin in the visible region of many biological tissues, which adversely affects the FI in the visible wavelength range. In particular, FI in the NIR-II range with weak absorption, scattering and autofluorescence of biological tissues can achieve deep penetration depth and tissue imaging in biological tissues. As a result, researchers are interested in the properties of NIR-II fluorescence that can be utilized for *in vivo* and nondestructive monitoring of tissues and are gradually introducing it into the diagnosis and treatment of cancer patients.[11–14]

To date, specific therapeutic modalities, such as photothermal therapy (PTT)[15–17] and photodynamic therapy (PDT)[18–21] based on reactive oxygen species (ROS),[22,23] have been developed to take advantage of the high level of acidic pH, endogenous H_2O_2, and overexpression of enzymes present in the tumor microenvironment. Among them, PTT has the advantages of short duration, significant efficacy, and low toxic side effects and has been partially applied in clinical practice. While the combination of NIR-II PTT and fluorescence imaging has a bright future of more precise diagnosis and improved therapeutic effects for tumors, the development of suitable conjugated polymers remain an obstacle in this field. To date, several

[a] Key Laboratory of New Processing Technology for Nonferrous Metal & Materials, Ministry of Education/Guangxi Key Laboratory of Optical and Electronic Materials and Devices, Guilin University of Technology, Guilin 541004, China. E-mail: lyuanli@glut.edu.cn

[b] State Key Laboratory of Organic Electronics and Information Displays & Institute of Advanced Materials (IAM), Jiangsu Key Laboratory for Biosensors, Nanjing University of Posts & Telecommunications, Nanjing 210023, China. E-mail: iampfsun@njupt.edu.cn

[c] CAS Key Laboratory of Soft Matter Chemistry, Department of Polymer Science and Engineering, University of Science and Technology of China, Jinzhai Road 96, Hefei 230026, China

† Electronic supplementary information (ESI) available. See DOI: https://doi.org/10.1039/d3tb00510k

classes of nanomaterials have been developed, including single-walled carbon nanotubes,[24,25] quantum dots,[26–28] rare earth materials,[29–31] small organic molecules,[32–37] and conjugated polymers.[38–40] However, the potential toxicity of inorganic nanomaterials *in vivo* and the poor processing and optical stability of organic small molecules greatly hinder their further clinical applications.[41–43] In contrast, low-bandgap conjugated polymers (CPs) have appeared as hopeful candidates for NIR FI due to their inherent ease of processing, spectral tunability, stability, and biocompatibility.[44] To date, conjugated polymers with both excellent properties of NIR-II PTT and NIR-II FI have seldom been reported due to their poor solubility in organic solutions, obvious quenching effect caused by aggregation, and powerful nonradiative decay, which invalidate the fluorescence emission of polymers.[45–47] Therefore, the rational design and manufacture of conjugated polymers for NIR-II FI/PTT is of great value in meeting the demands of accurate diagnosis as well as accurate and effective cancer therapy.

In this paper, a novel small squaric acid molecule with an emission wavelength in the near-infrared region was synthesized and coprecipitated with an amphiphilic block copolymer to obtain squaric acid nanoparticles with good biocompatibility. In addition, we introduced an azide group in the squaric acid small molecule and linked the water-soluble oligomer (POEGMA) to the squaric acid by a click chemistry reaction. As a result, we prepared a novel water-soluble squaric acid nanoparticle (SQ-POEGMA) with low toxicity and good photothermal effects in living organisms.

One major obstacle for this target is that significant fluorescence quenching will appear in water because of intense π–π stacking between squaraine dyes. First, SQ nanoparticles and SQ-POEGMA were synthesized through a condensation reaction according to our previous work.[48] As illustrated in Fig. 1a, the conjugation block consists of squaric acid as an electron acceptor and a fluorene-grafted thiophene segment as an electron donor. Meanwhile, each fluorene was modified with two azide-endcapped alkyl side chains to conjugate POEGMA, which endowed the water solubility of SQ-POEGMA. Then, water-dispersed SQ nanoparticles (SQ-NPs) were prepared by a coprecipitation method with an amphiphilic copolymer (PEG-*b*-PPG-*b*-PEG, F127). The chemical structures of SQ and SQ-POEGMA were characterized by ^{1}H NMR (Fig. S1–S5, ESI†). Transmission electron microscopy (TEM) (Fig. 1b) showed that SQ-POEGMA exhibited a spherical morphology. The size distribution of the particles in the TEM image is shown in Fig. 1c. The size distribution of the nanoparticles was in the range of 20–60 nm (Fig. 1c). Dynamic light scattering (DLS) results indicated that the hydrodynamic diameter (Dh) of SQ-POEGMA was 112 nm, which was different from the TEM results. Compared with the DLS results, the smaller size of the NPs in the TEM image was most likely due to the shrinkage of the NPs in the process of drying TEM samples. Then, the absorption and fluorescence emission spectra of SQ-NPs and SQ-POEGMA were measured to investigate their photophysical properties. A sharp and intense absorption peak of SQ-NPs in water was located at 660 nm with a shoulder peak at 745 nm

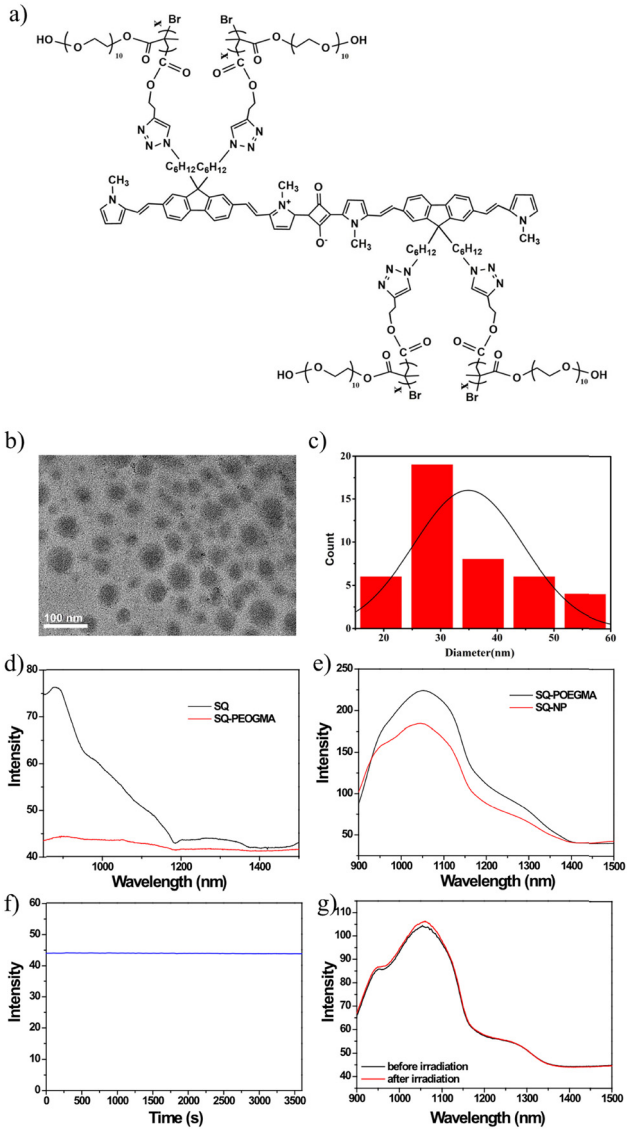

Fig. 1 Formulation and characterization of SQ-POEGMA. (a) Molecular structure of SQ-POEGMA. (b) TEM image of SQ-POEGMA nanoparticles. (c) The size distribution of the SQ-POEGMA. (d) Fluorescence spectra of SQ (0.1 mg mL^{-1}) and SQ-POEGMA (0.025 mg mL^{-1}) in THF under 808 nm irradiation. (e) Fluorescence spectra of SQ-NPS (0.03 mg mL^{-1}) and SQ-POEGMA (0.024 mg mL^{-1}) in aqueous solutions with equal absorption intensity. (f) Photostability of SQ-POEGMA under 808 nm irradiation for an hour (1.5 W cm^{-2}). (g) Fluorescence spectra of SQ-POEGMA after an hour irritation under 808 nm (1.5 W cm^{-2}).

(Fig. S7, ESI†). Compared with SQ-NPs, SQ-POEGMA displays different absorption behavior in water, displaying two similar intense peaks at 672 nm and 736 nm in water (Fig. S8, ESI†). The increased peak at 736 nm can be attributed to the alky chains and decreased aggregation. Fig. 1d and e show the emission spectra of SQ and SQ-POEGMA in THF and water with the same absorption intensity, respectively. The SQ-NPs showed significant fluorescence quenching in water due to intense π–π stacking. However, SQ-POEGMA maintained intense emission at 1055 nm with a tail that extended to 1400 nm in the NIR-II region. In addition, SQ-POEGMA

exhibited not only outstanding photostability (Fig. 1f and g) but also superior stability in physiological environments, including phosphate buffered saline (PBS), Dulbecco's modified Eagle's medium (DMEM), and fetal bovine serum (FBS), as shown in Fig. S10 (ESI†). Bright NIR-II fluorescence and excellent solubility in water indicated that SQ-POEGMA is a potential NIR-II imaging agent.

Based on the bright NIR-II fluorescence and brilliant stability in physiological environments, the NIR-II fluorescence imaging capacity of SQ-POEGMA was assessed under 808 nm excitation with a 1064 nm LP filter after tail vein injection of SQ-POEGMA aqueous solution (1.0 mg mL^{-1}). As depicted in Fig. 2a and b, the vasculature of the body was rapidly lit up, and then the belly and hind limb blood vessels could be clearly discriminated. The results showed that the signal to background ratios of the belly and hind limb blood vessels were calculated to be 4.4 and 6.7, and the signal-to-noise ratios were estimated to be 1.8 and 2.1, respectively. We further investigated the penetration depth of NIR-II persistent luminescence of SQ-POEGMA coated with different thicknesses of chicken tissue. Subsequently, a strong persistent luminescence signal was detected at the site of injection through 0.4 cm tissue thickness (S11, ESI†). The excellent *in vivo* image quality with high spatial resolution and contrast can be attributed to the lower photon scattering of NIR-II light. Fig. 2c illustrates the distribution change of SQ-POEGMA in the whole body over 48 h. The results clearly showed that large quantities of SQ-POEGMA were concentrated in the liver and spleen after intravenous injection. With time, SQ-POEGMA continuously accumulated around the MCF-7 tumor tissue and reached its peak at 24 h. To further confirm the biodistribution of SQ-POEGMA in mice, MCF-7 tumor-bearing mice were sacrificed at 48 h postinjection of SQ-POEGMA. The NIR-II fluorescence images of the tumor tissue and the main organs, including the heart, liver, spleen, lungs, and kidneys, illustrated that SQ-POEGMA mainly accumulated in the tumor tissue, liver and spleen (Fig. 2d and e). The great passive targeting capacity was mainly caused by their enhanced permeation and retention effect. In addition, the concentration-dependent photothermal effect will benefit from the high accumulation of SQ-POEGMA in the tumor tissue.

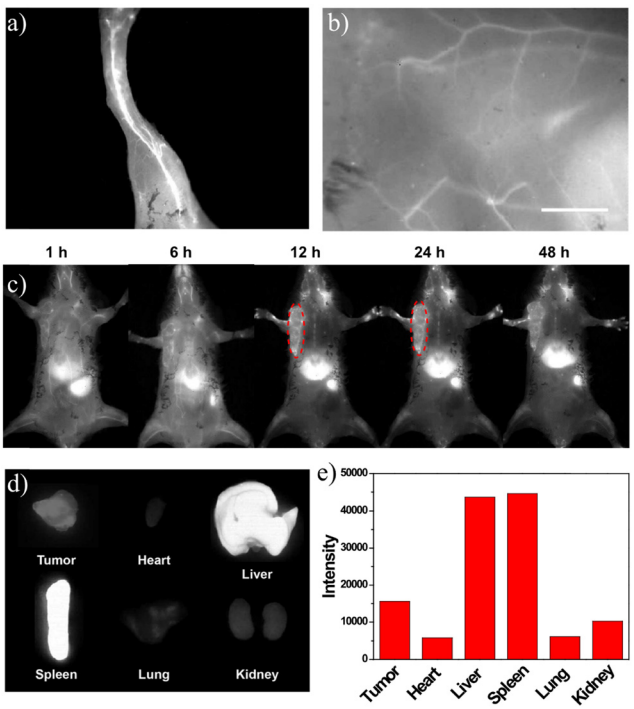

Fig. 2 NIR-II fluorescence images of mice intravenously injected at different postinjection times from one mouse. (a and b) NIR-II fluorescence images of the leg and abdomen. (c) *In vivo* NIR-II fluorescence images of MCF-7-bearing mice at different times after intravenous injection with SQ-POEGMA. (d) NIR-II fluorescence images of organ tissues at 24 h postinjection. (e) NIR-II quantified fluorescence intensity of organ tissues at 24 h postinjection.

The photothermal conversion and cytotoxicity of SQ-POEGMA *in vitro* were investigated as shown in Fig. 3a, which showed that the temperature of the SQ-POEGMA aqueous solution increased rapidly under 808 nm irradiation at a power density of 1.5 W cm^{-2} until it reached a plateau. The temperature changes of the 0.1 mg mL^{-1} and 0.04 mg mL^{-1} SQ-POEGMA aqueous solutions were 32 °C and 48 °C, respectively. The results also demonstrated that the maximum temperature of the SQ-POEGMA solutions depended on the concentration of SQ-POEGMA. According to the reported methods,[49] the photothermal conversion efficiency of SQ-POEGMA was calculated to be 33% (Fig. S6, ESI†). In addition, repeatable cycles of heating and natural cooling experiments demonstrated that SQ-POEGMA has superior photostability, as shown in Fig. 3b. To confirm effective cytotoxicity, the *in vitro* cellular uptake of SQ-POEGMA was investigated. SQ-POEGMA and MCF cells were cocultured for 12 h, and then the incubated and treated cells were collected for NIR-II imaging. As depicted in Fig. 3c, a strong fluorescence signal was observed in SQ-POEGMA cocultured cells, while a weak fluorescence signal was observed for the control group, demonstrating the excellent cellular uptake ability of SQ-POEGMA. Subsequently, the biocompatibility and photo cytotoxicity of SQ-POEGMA were evaluated *via* the standard 3-(4,5-dimethylthiazol-2-yl)-2,5-diphenyltetrazolium bromide (MTT) assay before exploring the *in vivo* performance. Fig. 3d shows that SQ-POEGMA displayed negligible cytotoxicity toward MCF-7 cells at a concentration of 120 μg mL^{-1}. The excellent biocompatibility of SQ-POEGMA can primarily be attributed to the good solubility and biocompatibility of the POEGMA segment. The MCF-7 cell viability decreased sharply under 808 nm irradiation with SQ-POEGMA concentrations from 7.5 μg mL^{-1} to 120 μg mL^{-1}. The IC50 of SQ-POEGMA upon 808 nm laser irradiation was calculated to be 26.59 μg mL^{-1}. MCF-7 cell injury demonstrates the notable photocytotoxicity of SQ-POEGMA. Moreover, confocal fluorescence imaging of calcein AM and propidium (PI) costained MCF-7 cancer cells indicated the excellent biocompatibility and high photocytotoxicity of SQ-POEGMA (Fig. 3e). MCF-7 cells exhibited high cell viability without 808 nm irradiation after 24 h incubation only with SQ-POEGMA, and cell injury did not occur for MCF-7 cells without SQ-POEGMA under 808 nm laser irradiation. However, MCF-7 cells cocultured with

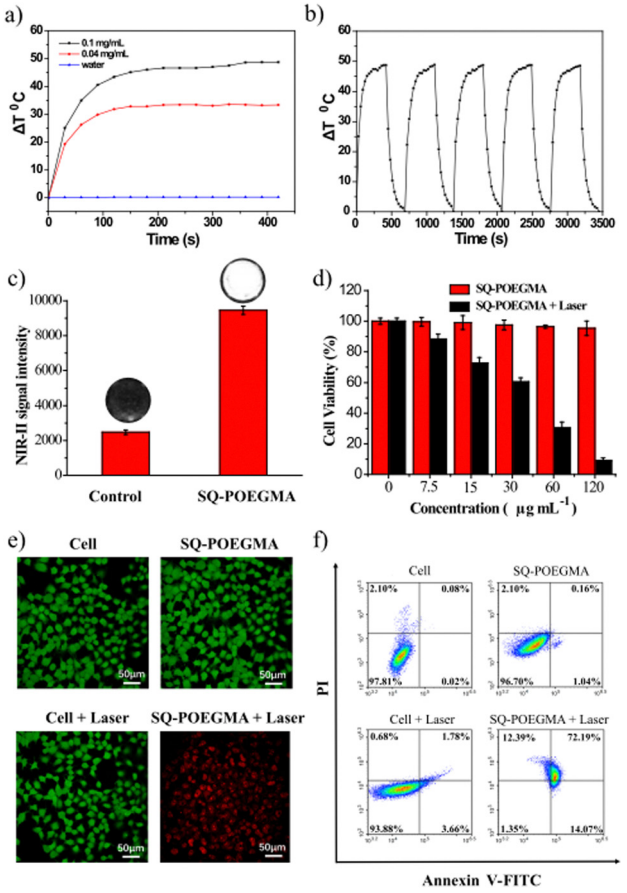

Fig. 3 Photothermal conversion and *in vitro* photothermal therapy of SQ-POEGMA. (a) Temperature elevation curves of SQ-POEGMA aqueous solution under 808 nm laser irradiation (1.5 W cm^{-2}) at different concentrations. (b) Temperature change curves of SQ-POEGMA (0.1 mg mL^{-1}) over the course of three cycles with discontinuous 808 nm laser irradiation (1.5 W cm^{-2}). (c) NIR-II fluorescence images and quantified signals of cancer cells without or with SQ-POEGMA. (d) Cell viabilities of MCF-7 cells with SQ-POEGMA for 24 h with or without 808 nm laser irradiation. (e) Calcein-AM/propidium iodide (PI) staining of MCF-7 cells incubated with SQ-POEGMA in the dark or exposed to 808 nm irradiation (1.5 W cm^{-2}) for 10 min. (f) Annexin V and PI staining for flow cytometry of MCF-7 cells with or without SQ-POEGMA under 808 nm irradiation (1.5 W cm^{-2}) for 10 min.

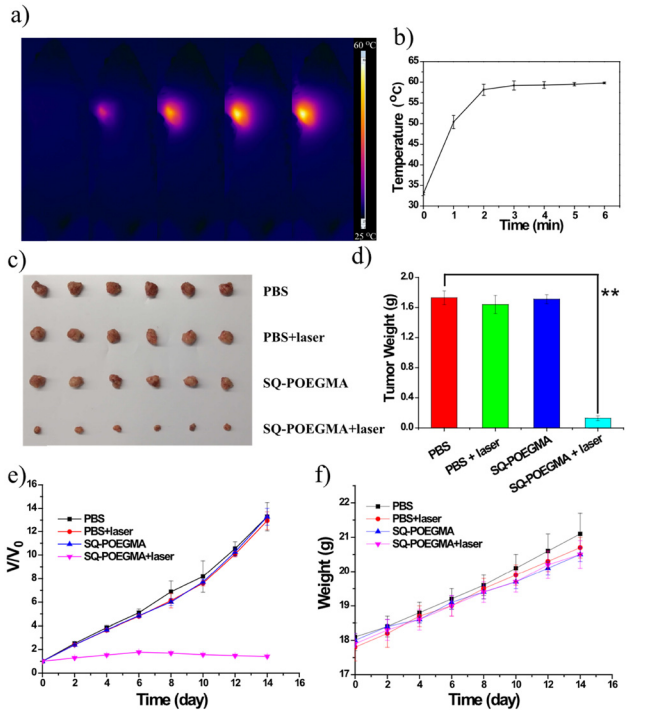

Fig. 4 Anticancer evaluation of SQ-POEGMA *in vivo*. (a) Thermal images of MCF-7 tumor-bearing mice 24 h postinjection of SQ-POEGMA aqueous solution under continuous 808 nm laser exposure at a power density of 1.5 W cm^{-2}. (b) Temperature elevation curves of the tumor. (c) Photographs of the tumors extracted from MCF-7 tumor-bearing mice at the end of PTT experiments. (d) Tumor weight of mice with MCF-7 tumors treated with the four treatment groups at the end of PTT experiments. (e) Body weight variation of MCF-7 tumor-bearing mice in different groups. The error bars represent the standard deviations of 5 mice per group. (f) Plots of tumor growth after different treatments. Tumor volumes were normalized to their original size.

SQ-POEGMA died after exposure to 808 nm irradiation (1.5 W cm^{-2}) for 10 min, which indicated that SQ-POEGMA possessed excellent photocytotoxicity under irradiation.

Inspired by the impressive results of FI, we investigated the PTT of the theranostic agent *in vivo*, and SQ-POEGMA was injected intravenously into subcutaneous xenograft tumors of mice. Depending on the time-point of maximum signals of the *in vivo* fluorescent imaging in the tumor site, PTT in living mice bearing MCF-7 breast tumors was carried out (12 h postinjection). An 808 nm laser (1.5 W cm^{-2}) was used to irradiate the tumor area in live mice for 6 minutes after intravenous administration of SQ-POEGMA (100 μL, 2 mg mL^{-1}) for 12 h. The temperature change in the laser-treated groups was recorded by a camera (Fig. 4a). The temperature of the tumor surface in the laser irradiation group rose rapidly from 36 °C to 55 °C in two minutes (Fig. 4b) proving that SQ-POEGMA exhibited an efficient NIR-II PTT effect. To further verify the PTT effect of SQ-POEGMA in living mice, the different treatments were conducted in four groups (n = 5 per group). The above four groups were denoted as (a) the control group treated with PBS, (b) the PBS with 808 nm laser excitation group (PBS + laser); (c) the only SQ-POEGMA group (SQ-POEGMA), and (d) the SQ-POEGMA with 808 nm laser irradiation group (SQ-POEGMA + laser). The tumors in the comparative groups (PBS, PBS + laser and SQ-POEGMA) rapidly increased by greater than 12.0-fold in 15 days, while the tumor volume of the "SQ-POEGMA + 808 nm" group, as depicted in Fig. 4d, was successfully inhibited after NIR-II PTT treatment with almost unchanged tumor size. The body weight and tumor growth for all groups of nude mice were checked every 2 days until 14 d, and no obvious weight loss was observed in the four groups (Fig. 4e and f), the tumor inhibition is calculated to be 94% suggesting high biocompatibility of PTT with SQ-POEGMA injection treatment. There was no significant damage to the normal tissues, including the liver, lungs, spleen, heart and kidneys, of PTT-treated mice (Fig. S12, ESI†).

In general, a water-soluble polymer nanoparticle SQ-POEGMA for precise NIR-II fluorescence imaging and efficient

NIR-II photothermal therapy was successfully synthesized, which exhibited excellent photothermal performance with a high photothermal conversion efficiency (PCE) of 33% and remarkable biocompatibility and high photocytotoxicity toward MCF-7 cells under 808 nm laser irradiation. Then, the fluorescence imaging properties of SQ-POEGMA were determined in mice, which clearly showed the blood vessels and organs in mice. Importantly, SQ-POEGMA can be applied as a competent phototheranostic probe for NIR-II FI-guided NIR-II PTT therapy to subcutaneous xenograft tumors. Furthermore, we believe that this work will provide effective guidance for designing novel NIR-II FI/NIR-II PTT phototheranostic agents.

Notes

All small animal experiments were carried out in accordance with the specifications of The National Regulation of China for Care and Use of Laboratory Animals, which have been approved by the Jiangsu Administration. Tumor-bearing mice (age 5–6 weeks) were purchased from KeyGEN BioTECH. Co., Ltd (Nanjing, China) with a pathogen-free feeding environment.

Conflicts of interest

The authors declare no conflict of interest.

Acknowledgements

This research was funded by the National Natural Science Foundation of China (Grant No. 21864010) and the Foundation of Key Laboratory of New Processing Technology for Nonferrous Metal & Materials, Ministry of Education/Guangxi Key Laboratory of Optical and Electronic Materials and Devices (Grant No. 22AA-6; 22KF-10).

References

1 L. F. Lin, Z. Y. Li, L. Yan, Y. L. Liu, H. J. Yang and H. Li, Global, regional, and national cancer incidence and death for 29 cancer groups in 2019 and trends analysis of the global cancer burden, 1990–2019, *J Hematol. Oncol.*, 2021, **14**(1), 1–24.

2 E. A. Sarma, S. C. Kobrin and M. J. Thompson, A Proposal to improve the early diagnosis of symptomatic cancers in the united states, *Cancer. Prev. Res.*, 2020, **13**(9), 715–719.

3 P. Mi, D. Kokuryo, H. Cabral, H. L. Wu, Y. Terada, T. Saga, I. Aoki, N. Nishiyama and K. Kataoka, A pH-activatable nanoparticle with signal-amplification capabilities for non-invasive imaging of tumour malignancy, *Nat. Nanotechnol.*, 2016, **11**(8), 724–730.

4 G. S. Hong, Y. P. Zou, A. L. Antaris, S. Diao, D. Wu, K. Cheng, X. D. Zhang, C. X. Chen, B. Liu, Y. H. He, J. Z. Wu, J. Yuan, B. Zhang, Z. M. Tao, C. Fukunaga and H. J. Dai, Ultrafast fluorescence imaging *in vivo* with conjugated polymer fluorophores in the second near-infrared window, *Nat. Commun.*, 2014, **5**(1), 1–9.

5 M. A. Sowers, J. R. McCombs, Y. Wang, J. T. Paletta, S. W. Morton, E. C. Dreaden, M. D. Boska, M. F. Ottaviani, P. T. Hammond, A. Rajca and J. A. Johnsons, Redox-responsive branched-bottlebrush polymers for *in vivo* MRI and fluorescence imaging, *Nat. Commun.*, 2014, **5**(5), 5460.

6 J. L. Bridot, A. C. Faure, S. Laurent, C. Rivière, C. Billotey, B. Hiba, M. Janier, V. Josserand, J. L. Coll, L. V. Elst, R. Muller, S. Roux, P. Perriat and O. Tillement, Hybrid gadolinium oxide nanoparticles: multimodal contrast agents for *in vivo* imaging, *J. Am. Chem. Soc.*, 2007, **129**(16), 5076–5084.

7 T. Imamura, T. Saitou and R. Kawakami, *In vivo* optical imaging of cancer cell function and tumor microenvironment, *Cancer Sci.*, 2018, **109**(4), 912–918.

8 M. H. Y. Cheng, K. M. Harmatys, D. M. Charron, J. Chen and G. Zheng, Stable j-aggregation of an aza-BODIPY-lipid in a liposome for optical cancer imaging, *Angew. Chem., Int. Ed.*, 2019, **131**(38), 13528–13533.

9 J. E. Schaik, G. B. Halmos, M. J. H. Witjes and B. E. C. Plaat, An overview of the current clinical status of optical imaging in head and neck cancer with a focus on Narrow Band imaging and fluorescence optical imaging, *Oral Oncol.*, 2021, **121**, 105504.

10 E. Winckel, M. Mascaraque, A. Zamarron, A. J. Fuente, T. Torres and A. Escosura., Dual role of subphthalocyanine dyes for optical imaging and therapy of cancer, *Adv. Funct. Mater.*, 2018, **28**(24), 1705938.

11 X. B. Zhou, Q. Liu, W. Yuan, Z. H. Li, Y. L. Xu, W. Feng, C. J. Xu and F. Y. Li, Ultrabright NIR-II emissive polymer dots for metastatic ovarian cancer detection, *Adv. Sci.*, 2021, **8**(4), 2000441.

12 W. H. Xu, D. Wang and B. Z. Tang, NIR-II AIEgens: a win-win integration towards bioapplications, *Angew. Chem., Int. Ed.*, 2021, **133**(14), 7552–7563.

13 H. Wu, H. H. Wu, Y. N. He, Z. Gan, Z. L. Xu, M. Zhou, S. Liu and H. M. Liu, Synovitis in mice with inflammatory arthritis monitored with quantitative analysis of dynamic contrast-enhanced NIR fluorescence imaging using iRGD-targeted liposomes as fluorescence probes, *Int. J. Nanomed.*, 2018, **13**, 1841.

14 C. P. Ding, Y. J. Huang, Z. Y. Shen and X. Y. Chen, Synthesis and bioapplications of Ag_2S quantum dots with near-infrared fluorescence, *Adv. Mater.*, 2021, **33**(32), 2007768.

15 Y. T. Zhao, L. P. Tong, Z. B. Li, N. Yang, H. D. Fu, L. Wu, H. D. Cui, W. H. Zhou, J. H. Wang, H. Y. Wang, P. K. Chu and X. F. Yu, Stable and multifunctional dye-modified black phosphorus nanosheets for near-infrared imaging-guided photothermal therapy, *Chem. Mater.*, 2017, **29**(17), 7131–7139.

16 B. Shi, Q. Yan, J. Tang, K. Xin, J. Zhang, Y. Zhu, G. Xu, R. C. Wang, J. Chen, W. Gao, T. L. Zhu, J. Y. Shi, C. H. Fan, C. C. Zhao and H. Tian, Hydrogen sulfide-activatable second near-infrared fluorescent nanoassemblies for targeted photothermal cancer therapy, *Nano Lett.*, 2018, **18**(10), 6411–6416.

17 A. S. Moses, O. R. Taratula, H. Lee, F. Z. Luo, T. Grenz, T. Korzun, A. S. Lorenz, F. Y. Sabei, S. Bracha, A. W. G. Alani,

O. D. Slayden and O. Taratula, Nanoparticle-Based Platform for Activatable Fluorescence Imaging and Photothermal Ablation of Endometriosis, *Small*, 2020, **16**(18), 1906936.

18 P. Tao, Z. Lv, X. K. Zheng, H. Jiang, S. Liu, H. Wang, W. Y. Wong and Q. Zhao, Isomer engineering of lepidine-based iridophosphors for far-red hypoxia imaging and photodynamic therapy, *Inorg Chem.*, 2022, **61**(44), 17703–17712.

19 Y. Zhou, X. Ren, Z. Hou, N. Wang, Y. Jiang and Y. Luan, Engineering a photosensitizer nanoplatform for amplified photodynamic immunotherapy via tumor microenvironment modulation, *Nanoscale Horiz.*, 2021, **6**(2), 120–131.

20 M. Yu, R. Cao, Z. Ma and M. Zhu, Development of ''smart'' drug delivery systems for chemo/PDT synergistic treatment, *J. Mater. Chem. B*, 2023, **11**, 1416–1433.

21 X. Liu, N. Xu, X. M. Pu, J. Wang, X. M. Liao, Z. B. Huang and G. F. Yin, Combined photothermal–photodynamic therapy by indocyanine green loaded polydopamine nanoparticles enhances anti-mammary gland tumor efficacy, *J. Mater. Chem. B*, 2022, **10**(24), 4605–4614.

22 Y. J. Wang, X. J. Sun, Y. Chang and H. Y. Zhang, Energy transfer facilitated near infrared fluorescence imaging and photodynamic therapy of tumors, *Biomat. Sci.*, 2021, **9**(13), 4662–4670.

23 J. Li, Z. P. Zhu, S. Q. Rong, H. R. Li, Y. N. Guo, Q. Xue and D. Ding, A specific environment-sensitive near-infrared fluorescent turn-on probe for synergistic enhancement of anticancer activity of a chemo-drug, *Biomater. Sci.*, 2017, **5**(8), 1622–1628.

24 G. S. Hong, J. C. Lee, J. T. Robinson, U. Raaz, L. M. Xie, N. F. Huang, J. P. Cooke and H. J. Dai, Multifunctional *in vivo* vascular imaging using near-infrared II fluorescence, *Nat. Med.*, 2012, **18**(12), 1841–1846.

25 G. S. Hong, S. Diao, J. L. Chang, A. L. Antaris, C. X. Chen, B. Zhang, S. Zhao, D. N. Atochin, P. L. Huang, K. I. Andreasson, C. J. Kuo and H. J. Dai, Through-skull fluorescence imaging of the brain in a new near-infrared window, *Nat. Photonics*, 2014, **8**(9), 723–730.

26 D. H. Zhao, X. Q. Yang, X. L. Hou, Y. Xuan, X. L. Song, Y. D. Zhao, W. Chen, Q. Wang and B. Liu, *In situ* aqueous synthesis of genetically engineered polypeptide-capped Ag_2S quantum dots for second near-infrared fluorescence/photoacoustic imaging and photothermal therapy, *J. Mater. Chem. B.*, 2019, **7**(15), 2484–2492.

27 A. Zebibula, N. Alifu, L. Q. Xia, C. W. Sun, X. M. Yu, D. W. Xue, L. W. Liu, G. H. Li and J. Qian, Ultrastable and Biocompatible NIR-II Quantum Dots for Functional Bioimaging, *Adv. Funct. Mater.*, 2018, **28**(9), 1703451.

28 J. Y. Li, T. Y. Guan, D. T. Tu, W. Lian, P. Zhang, S. Y. Han, F. Wen and X. Y. Chen, Highly efficient NIR-II luminescent I-III-VI semiconductor nanoprobes based on $AgInTe_2$:Zn/ZnS nanocrystals, *Chem. Commun.*, 2022, **58**(13), 2204–2207.

29 D. J. Naczynski, M. C. Tan,M. Zevon,B. Wall, J. Kohl, A. Kulesa, S. Chen, C. M. Roth, R. E. Riman and P. V. Moghe, Rare-earth-doped biological composites as *in vivo* shortwave infrared reporters, *Nat. Commun.*, 2013, **4**(1), 1–10.

30 X. Zhang, S. Q. He, B. B. Ding, C. R. Qu, Q. Zhang, H. Chen, Y. Sun, H. Y. Fang, Y. Long, R. P. Zhang, X. L. Lan and Z. Cheng, Cancer cell membrane-coated rare earth doped nanoparticles for tumor surgery navigation in NIR-II imaging window, *Chem. Eng. J.*, 2020, **385**, 123959.

31 Z. Liu, F. Ren, H. Zhang, Q. Yuan, Z. L. Jiang, H. H. Liu, Q. Sun and Z. Li, Boosting often overlooked long wavelength emissions of rare-earth nanoparticles for NIR-II fluorescence imaging of orthotopic glioblastoma, *Biomaterials*, 2019, **219**, 119364.

32 Q. Wang, B. Xia, J. Z. Xu, X. R. Niu, J. Cai, Q. M. Shen, W. J. Wang, W. Huang and Q. L. Fan, Biocompatible small organic molecule phototheranostics for NIR-II fluorescence/photoacoustic imaging and simultaneous photodynamic/photothermal combination therapy, *Mater. Chem. Front.*, 2019, **3**(4), 650–655.

33 Q. Wang, X. R. Niu, L. Q. Yang, J. W. Liu, J. Wang, X. P. Xu, W. H. Tang, W. Huang and Q. L. Fan, Asymmetric small organic molecule-based NIR-II fluorophores for high performance tumor phototheranostics, *Mater. Chem. Front.*, 2021, **5**(15), 5689–5697.

34 Y. X. Li, H. L. Zhou, R. Z. Bi, X. T. Li, M. L. Zha, Y. Q. Yang, J. S. Ni, W. H. Liew, M. Olivo, K. Yao, J. Liu, H. Chen and K. Li, Acceptor engineering of small-molecule fluorophores for NIR-II fluorescence and photoacoustic imaging, *J. of Mater. Chemistry B*, 2021, **9**(48), 9951–9960.

35 W. Wu, Y. Q. Yang, Y. Yang, Y. M. Yang, K. Y. Zhang, L. Guo, H. F. Ge, X. W. Chen, J. Liu and H. Feng, Molecular engineering of an organic NIR-II fluorophore with aggregation-induced emission characteristics for *in vivo* imaging, *Small*, 2019, **15**(20), 1805549.

36 Q. L. Yang, Z. B. Hu, S. J. Zhu, R. Ma, H. L. Ma, Z. R. Ma, H. Wan, T. Zhu, Z. Y. Jiang, W. Q. Liu, L. Y. Jiao, H. T. Sun, Y. Y. Liang and H. J. Dai, Donor engineering for NIR-II molecular fluorophores with enhanced fluorescent performance, *J. Am. Chem. Soc.*, 2018, **140**(5), 1715–1724.

37 H. L. Ma, C. C. Liu, Z. B. Hu, P. P. Yu, X. F. Zhu, R. Ma, Z. R. Sun, C. H. Zhang, H. Sun, S. J. Zhu and Y. Y. Liang, Propylenedioxy thiophene donor to achieve NIR-II molecular fluorophores with enhanced brightness, *Chem. Mater.*, 2020, **32**(5), 2061–2069.

38 X. W. Song, X. M. Lu, B. Sun, H. Zhang, P. F. Sun, H. Miao, Q. L. Fan and W. Huang, Conjugated polymer nanoparticles with absorption beyond 1000 nm for NIR-II fluorescence imaging system guided NIR-II photothermal therapy, *ACS. Appl. Polym. Mater*, 2020, **2**(10), 4171–4179.

39 X. M. Lu, P. C. Yuan, W. S. Zhang, Q. Wu, X. X. Wang, M. Zhao, P. F. Sun, W. Huang and Q. L. Fan, A highly water-soluble triblock conjugated polymer for *in vivo* NIR-II imaging and photothermal therapy of cancer, *Polym. Chem.*, 2018, **9**(22), 3118–3126.

40 Y. Chen, B. Sun, X. Y. Jiang, Z. Y. Yuan, S. Y. Chen, P. F. Sun, Q. L. Fan and W. Huang, Double-acceptor conjugated polymers for NIR-II fluorescence imaging and NIR-II photothermal therapy applications, *J. Mater. Chem. B.*, 2021, **9**(4), 1002–1008.

41 D. Y. Li, D. Wang, X. Y. Zhao, W. Xi, A. Zebibula, N. Alifu, J. F. Chen and J. Qian, Short-wave infrared emitted/excited fluorescence from carbon dots and preliminary applications in bioimaging, *Mater. Chem. Front.*, 2018, **2**(7), 1343–1350.

42 Q. l Yang, Z. R. Ma, H. H. Wang, B. Zhou, S. J. Zhu, Y. T. Zhong, J. Y. Wang, H. Wan, A. Antaris, R. Ma, X. Zhang, J. Y. Yang, X. D. Zhang, H. T. Sun, W. Q. Liu, Y. Y. Liang and H. J. Dai, Rational Design of Molecular Fluorophores for Biological Imaging in the NIR-II Window, *Adv. Mater.*, 2017, **29**(12), 1605497.

43 A. L. Antaris, H. Chen, K. Cheng, Y. Sun, G. S. Zhang, X. D. Zhang, O. K. Yaghi, Z. R. Alamparambil, X. Ch Hong, Z. Cheng and H. J. Dai, A small-molecule dye for NIR-II imaging, *Nat. Mater.*, 2016, **15**(2), 235–242.

44 B. Guo, Z. H. Sheng, D. H. Hu, A. Li, S. D. Xu, P. N. Manghnani, C. B. Liu, L. Guo, H. Zheng and B. Liu, Molecular engineering of conjugated polymers for biocompatible organic nanoparticles with highly efficient photoacoustic and photothermal performance in cancer theranostics, *ACS Nano*, 2017, **11**(10), 10124–10134.

45 Y. H. Li, Y. X. Wu, J. T. Chen, J. L. Wan, C. Xiao, J. K. Guan, X. L. Song, S. Y. Li, M. M. Zhang, H. C. Cui, T. T. Li, X. Q. Yang, Z. F. Li and X. L. Yang, A simple glutathione-responsive turn-on theranostic nanoparticle for dual-modal imaging and chemo-photothermal combination therapy, *Nano Lett.*, 2019, **19**(8), 5806–5817.

46 W. S. Zhang, W. X. Deng, H. Zhang, X. L. Sun, T. Huang, W. J. Wang, P. F. Sun, Q. L. Fan and W. Huang, Bioorthogonal-targeted 1064 nm excitation theranostic nanoplatform for precise NIR-IIa fluorescence imaging guided efficient NIR-II photothermal therapy, *Biomaterials*, 2020, **243**, 119934.

47 X. W. Song, X. M. Lu, B. Sun, H. Zhang, P. F. Sun, H. Miao, Q. L. Fan and W. Huang, Conjugated polymer nanoparticles with absorption beyond 1000 nm for NIR-II fluorescence imaging system guided NIR-II photothermal therapy, *ACS Appl. Polym. Mater.*, 2020, **2**(10), 4171–4179.

48 P. F. Sun, Q. Wu, X. L. Sun, H. Miao, W. X. Deng, W. S. Zhang, Q. L. Fan and W. Huang, J-Aggregate squaraine nanoparticles with bright NIR-II fluorescence for imaging guided photothermal therapy, *Chem. Commun.*, 2018, **54**(95), 13395–13398.

49 D. Keith Roper, W. Ahn and M. Hoepfner, Microscale heat transfer transduced by surface plasmon resonant gold nanoparticles, *J. Phys. Chem. C*, 2007, **111**(9), 3636–3641.